




EUV Spectra and Line Ratios of Multiply Ionized Calcium and Argon Atoms in a Laboratory Plasma

Elmar Träbert^{1,2} , Peter Beiersdorfer¹ , Jaan K. Lepson³, Matthew L. Reinke⁴, and John E. Rice⁵

¹ Physics Division, Physical and Life Sciences, Lawrence Livermore National Laboratory, Livermore, CA 94550-9234, USA

² Astronomisches Institut, Ruhr-Universität Bochum, 44780 Bochum, Germany

³ Space Sciences Laboratory, University of California, Berkeley, CA 94721, USA

⁴ Oak Ridge National Laboratory, Oak Ridge, TN 37830, USA

⁵ Plasma Science and Fusion Center, MIT, Cambridge, MA 02139, USA

Received 2018 June 28; revised 2018 August 8; accepted 2018 August 17; published 2018 October 3

Abstract

The utility of Ca in the EUV spectral range of astrophysical observations is limited by a fragmentary and incomplete record of laboratory data. In order to obtain a more comprehensive survey of the Ca line emission in the EUV, we have used a tokamak plasma discharge in hydrogen carrying some Ar and intermittently seeded with Ca as a tool for investigating the emission line intensity pattern of highly charged Ca and Ar ions in the wavelength range 100–285 Å with 0.35 Å spectral resolution. We compare our data to wavelengths and line ratios in much-used databases, especially CHIANTI, and we discuss apparent inconsistencies.

Key words: atomic data – methods: laboratory: atomic

1. Introduction

Calcium has a nuclear charge (Ca, $Z = 20$) just two units higher than that of argon (Ar, $Z = 18$), and the two elements have similar cosmic abundances. Hence in astrophysical spectra the two elements might be expected to be similarly excited. If a line ratio of interest is affected by observational problems in one element, the corresponding lines might be accessible in the other. However, the coverage of the two elements varies considerably across wavelength databases, as does the extent and quality of auxiliary information, if any. For example, Kelly (1987) has compiled spectral data from many plasma experiments. Among these are 308 spectral lines of Ca V through Ca XX in the wavelength range 100–300 Å. The NIST ASD database (Kramida et al. 2017; <http://physics.nist.gov/asd>), however, lists only 46 spectral lines of the same spectra in the same wavelength range. Among the missing lines are ground-state transitions in few-electron ions that are expected to be rather prominent in spectra. Ar, in contrast, has more lines in these compilations. Many hundreds more lines of Ar and Ca have been presented by the CHIANTI project (Dere et al. 1997, 2009; Landi et al. 2012, 2013; Del Zanna et al. 2015; <http://www.chiantidatabase.org/>), but many (if not most) of the additional lines are from computations and have not yet been confirmed by observation. We note that the CHIANTI wavelength listings state four decimals after the point, seemingly implying a precision of 0.1 mÅ, which generally is not substantiated by the experimental evidence. In particular, some of their Ar X listings differ from the much earlier data compiled by Kelly (1987) by significantly more than 0.1 Å, i.e., by three orders of magnitude more than the apparent uncertainty. These specific differences have recently been corroborated in high-resolution spectra recorded at an electron beam ion trap (Beiersdorfer & Träbert 2017) in favor of the values given by Kelly (1987). This example shows that database entries can be inaccurate by amounts that substantially exceed the implied uncertainty or the typical experimental uncertainty, which in the EUV is closer to 10–50 mÅ. Beyond the possibility of computational and clerical error, one has to keep in mind that although many solar spectra have been

recorded with excellent spectral resolution, they contain lines from many elements, and misidentifications are possible.

There are, of course, more databases available than the three examples mentioned above. For example, Foster et al. (2012) mention the “three widely used atomic databases”: SPEX v2.0 (Kaastra et al. 1996), CHIANTI v7 (Landi et al. 2012), and AtomDB v1.3.1 (Smith et al. 2001). Evidently two of these are about two decades old by now and likely in need of updates. The third database is being updated by virtue of the above cited paper, which actually introduces AtomDB v2.0.2 as using CHIANTI v7 of the same year 2012. The CHIANTI v8 that we use has been available since 2015. AtomDB v3 has since been mentioned at conferences. The AtomDB database evidently is not independent; it relies on previously published versions of the CHIANTI database and consequently tends to lag behind. Another astrophysically reputed website for spectrum simulations is Cloudy (<https://www.nublado.org>); the Cloudy project emphasizes photoionization processes and specific influences of the interstellar environment, which are of lesser concern to us. The CHIANTI “atomic database for spectroscopic diagnostics of astrophysical plasmas” is primarily designed to help understanding the solar EUV spectrum and thus matches most closely our experiment and scope. It provides wavelengths and transition rates as well as relative line intensities, computed for the optimum production energy of a given spectrum and for various plasma densities. The line ratios from the model are expected to be more appropriate than the results of the basic quantum mechanical treatment by White & Eliasson (1933) which refers to the case of statistical level population (implying local thermodynamic equilibrium) and small fine structure intervals, but yields a good first estimate anyway. Those relative line intensities should help to narrow down the choices when trying to analyze solar spectra. The CHIANTI listings contribute the most to the literature data we compare our measurements to. By the way, the cross section data on ions of various isoelectronic sequences as stored in the CHIANTI database have recently been critically reviewed by Feldman (2016).

The aforementioned unclear situation of spectral EUV data on Ca may have misled Raassen et al. (2002) in their analysis of X-ray spectra from *Chandra* and *XMM-Newton* to assign several weak features above $\lambda 100$ to this element; these lines have since been identified with iron (Beiersdorfer et al. 2014a). It is likely that the strongest lines of Ca have been identified correctly in the laboratory about half a century ago by various authors, whose analysis was then supported by Cowan code computations. However, there are many sizeable differences between the wavelengths compiled then (Kelly 1987) and listed now (Del Zanna et al. 2015). Considering the aforementioned shortcomings of Ca data tables in the extreme ultraviolet spectral range, it seems advantageous to measure these lines in the laboratory. Here we present measurements that were performed at the Alcator C-Mod tokamak (Marmar et al. 2015). Tokamak plasma consists of hydrogen or helium, and it contains only trace amounts of heavier elements. In particular, Ar is generally added in order to facilitate spectroscopic diagnostics in the X-ray range (Hill et al. 2008). In our experiment, Ca and F⁶ were added to this mixture during the discharge by laser pulses heating a target of CaF₂. Our spectrograph on Alcator had a wide spectral coverage that ascertained that the observations included some unequivocally identified Ca lines. At the same time, Ar with its similar EUV spectrum (but systematically displaced toward longer wavelengths) served as a comparison. This combination served as a test of the CHIANTI spectral model in terms of wavelengths as well as line ratios.

2. Measurement and Data Evaluation

The Alcator C-Mod tokamak at the Massachusetts Institute of Technology (MIT) (Marmar 2007) features a torus-shaped plasma vessel. The plasma is confined by externally and internally generated magnetic fields and can be heated by various processes. The plasma can reach a temperature in the range of several keV, while for our data set, the plasma core was at $T_e \approx 1.7$ keV. The electron density of $n_e \approx 10^{14}$ cm⁻³ exceeds the dilute plasma conditions of stellar coronae by several orders of magnitude, but is consistent with flare conditions; among laboratory plasma experiments, tokamaks qualify as devices of relatively low density. For EUV spectroscopic monitoring, flat-field spectrographs equipped with CCD detectors have been attached to the vacuum vessel (Graf et al. 2008). Of two widely used basic versions, the XEUS instrument (X-ray and Extreme Ultraviolet Spectrometer) is mostly used for wavelengths below 100 Å. It has an $R = 15$ m diffraction grating with about 2400 ℓ/mm , and its use on Alcator C-Mod, as well as many operational details that also pertain to the present measurements (shot 1120620024T), have been described by Reinke et al. (2010) and Beiersdorfer et al. (2011). The presently used LoWEUS instrument (Long-wavelength Extreme Ultraviolet Spectrometer; Lepson et al. 2016; Weller et al. 2016) features a 1200 ℓ/mm $R = 5$ m grating operating at an angle of incidence of 87° and a 1340 × 1000 pixel (of 20 $\mu\text{m} \times 20 \mu\text{m}$ each) cryogenically cooled CCD chip with a spectral resolution of about 0.35 Å. As positioned for our measurement, the spectral range was 100–285 Å. Similar

instruments have been used in laboratory astrophysics studies at the Livermore EBIT facility (Beiersdorfer et al. 1999; Beiersdorfer 2003; Lepson et al. 2003, 2005a, 2005b) and are in use at the NSTX, DIII-D, and LTX tokamaks (Graf et al. 2008; Lepson et al. 2010, 2012, 2013; Weller et al. 2016; Victor et al. 2017). By previous experience with these instruments, the appearance of some higher-diffraction order lines is likely and may contribute to some of our unidentified lines.

The basic discharge gas in the Alcator C-Mod experiment was deuterium (D₂). In our spectral range, He II lines Ly _{β} ($\lambda 256$), Ly _{γ} ($\lambda 243$), and Ly _{δ} ($\lambda 233$) indicated traces of He remaining from preceding experiments. Both elements, H and He, have little or no line emission in the wavelength range of present interest, and the spectrum was dominated by several heavier elements such as Mo ($Z = 42$), Ca ($Z = 20$), and Ar ($Z = 18$), plus a few weak contributions from O ($Z = 8$), N ($Z = 7$), and C ($Z = 6$). Of these elements only Ar and Ca were employed intentionally and will be discussed in more detail in the subsequent section.

Mo atoms originated from molybdenum-covered tiles that protect parts of the vacuum vessel that might be exposed to the hot plasma resulting in sputtering, the production of highly charged ions, and excitation of their spectra. Highly ionized Mo (spectra Mo XXXI and Mo XXXII) has been reported from Alcator C-Mod before (Rice et al. 1996; Reinke et al. 2010), as well as from the JET tokamak (Jupén et al. 1990; Ekberg et al. 1991). We have tried to minimize, if not fully avoid, the Mo lines in our data by selecting suitable time frames.

An internal target made of CaF₂ was used to introduce F and Ca by laser ablation (Howard et al. 2011). The laser firings were spaced by about 0.1 s in the middle of the plasma discharges that lasted about 2 s each. Every 2 ms a spectrum was read out from the full chip, but binned in the direction orthogonal to the spectral dispersion, so that about 1000 successive spectra covered a single plasma discharge. To condense the data into fewer spectra and to reduce the statistical scatter before visual inspection, every 10 spectra were binned, essentially reducing the time resolution in our analysis to 20 ms.

Figure 1 shows the total signal summed over wavelength and divided by the number of channels to obtain an average as a function of time. Clearly the plasma discharge evolves through phases. In the initial phase (the first 0.5 s), before the plasma is diverted, the plasma emission is dominated by spectral lines of various impurities, among which is highly ionized Mo. This indicates that the hot plasma touches Mo-coated surfaces, which provide cold, neutral atoms that are rapidly ionized up to charge states with ionization potentials close to 4 keV (Reinke et al. 2010). When the initial plasma formation phase has subsided and wall contact is diminished, the sum signal for more than 1 s remains on a plateau much lower than the initial signal burst (see Figure 1). In this phase, a pulsed laser is used to inject material from a CaF₂ target inside the discharge vessel. Figure 1 shows nine such injections of almost equal efficacy. This figure cannot distinguish between photons from just the injected (and ionized) material and an overall plasma emission that increases because of the plasma perturbation (a slight lowering of the electron temperature accompanied by increased emission) caused by the ablation of CaF₂. However, wavelength spectra of the plasma in this phase (Figure 2) reveal that the brightest lines now result from highly ionized Ar and Ca atoms, with Ca present only during injection. By this time the

⁶ The literature situation for spectral data on F is as uneven as that for Ca: Kelly (1987) lists many measured F lines in the EUV; CHIANTI does not list F at all, because it is of little solar interest, and the NIST ASD holdings on F have been very slim in comparison to the neighboring elements O and Ne until rather recently, when they were boosted by adding computed results.

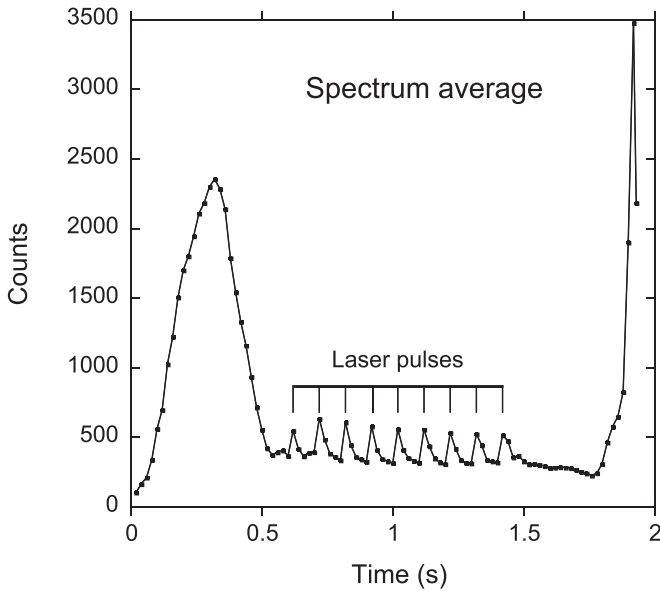


Figure 1. Signal (averaged over all wavelength channels) as a function of time (averaged over 10 time channels). The plasma emission is brightest in the first 0.5 s, before the plasma is diverted (which reduces the influx of impurities). In the middle, nine laser pulses spaced by 0.1 s add material by ablation of CaF_2 . In the end, the plasma recombines before the discharge ceases.

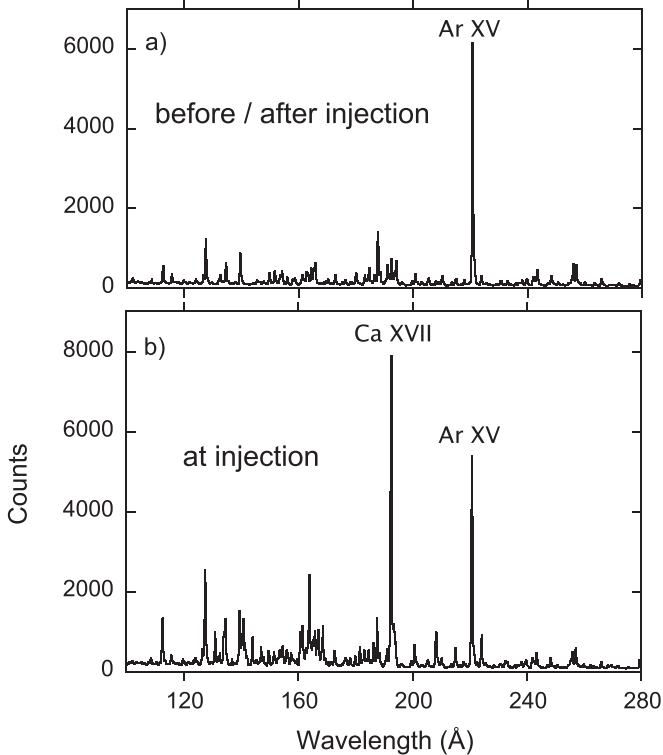


Figure 2. Sample spectra after plasma formation and stabilization (near $t \approx 0.8$ s), (a) immediately before CaF_2 injection (optimizing Ar), and (b) during CaF_2 laser ablation (peak Ca signal).

Mo lines have decreased markedly in number and intensity, but the number of lines discriminated by a multipeak fit routine remains close to 100. This is the discharge phase most suitable for studying the spectra of the element of primary interest, that is, Ca. Near the end of the discharge, after about 1.8 s, the overall light emission curve rises again and even exceeds the initial burst. This late plasma recombination phase is dominated

by Ar line emission and a continuum-like background. After a steep rise in signal, the discharge ends.

3. Data and Analysis

The LoWEUS spectrograph serves as a routine spectrum monitor, the settings of which are changed only occasionally. Thus a calibration curve was established earlier, and this wavelength scale checked against a number of known lines that appear in the data. The primary sources of reference data were the compilations by Kelly (1987), NIST (Kramida et al. 2017), and CHIANTI version 8 (Del Zanna et al. 2015). However, as we have mentioned earlier, many of the CHIANTI entries result from computations only, and these have been disregarded here. Due to our spectral resolving power and the presence of many line blends, our wavelength determinations are limited to uncertainties of about 20 mÅ.

The results of our analysis are presented in three tables. Table 1 presents Ca and lists a few Ar lines that blend with Ca lines. The data (see Figure 3) were obtained at the time of maximum Ca abundance during laser injection. Table 2 presents Ar at a time just before laser injection (see Figure 4), that is, of minimum (if any) presence of Ca. There nevertheless are line blends with other—often unrecognized—elements, and Table 3 indicates such foreign (neither clearly Ca nor Ar) or unidentified lines. Not all lines listed elsewhere appear in our data. One cause of uncertainty is the CHIANTI modeling process for specific electron densities, which does not necessarily give a reliable threshold above which lines might be considered bright enough to see. In some cases, we see a line much stronger than predicted for Ar or Ca, but we cannot determine the line identity. In others, lines are missing from a predicted line group, which casts doubt on the model computation. As usual, weak lines are most numerous and thus fare a higher probability of line blends. The time history of the discharge offers clues to the elemental identity of unknown lines. Mo and some light elements (C, N, O) appear almost only early in the discharge and are easily identified from spectral tables such as the Kelly tables (Kelly 1987) or the NIST ASD database (Kramida et al. 2017). F and Ca are expected only during the injection phase, while the Ar signal (Ar being part of the gas mixture) appears throughout the discharge, increasing in intensity after the initial phase, and shows a further increase late in the discharge. Illustrating figures are discussed below.

The core temperature in Alcator C-Mod was almost 2 keV, much higher than the complete ionization potentials of the light elements, which are below 1 keV. The most prominent lines of Ca and Ar in our spectra are from their Be-like ions, which have ionization potentials of 1.09 keV and 0.86 keV, respectively. Consequently, the signal from lighter ions (C, N, O) disappears soon (“burning out”), a consequence of rapid ionization up to and beyond the ionization stages that might contribute to the signal in the present spectral working range. Because of changes in the elemental composition, the “effective atomic number” Z_{eff} varies from 3.4 at the beginning to 1.4 at the end of the first discharge phase. By selecting observations after the start-up phase and right after Ca injection, we can largely disregard Mo and a number of light gases. In order to maximize the signal of Ca, we choose spectra at the first and second laser injection peak for the discussion below, and the average of the signals at the two peaks for our line intensities of Ca.

Table 1
Lines Observed in the Wavelength Band $\lambda 100$ to $\lambda 285$ in the Injection Phase of the Tokamak Plasma

Spectrum	Transition	Wavelength ^a (Å)	Rel. Int. ^a	Wavelength ^b (Å)	Rel. Int. ^c	Wavelength ^d (Å)
Be-like: Ca XVII						
Ca XVII	$2s^2\ ^1S_0-2s2p\ ^1P_1^o$	192.83	7160	192.8532	1000	...
Ca XVII	$2s2p\ ^3P_1^o-2p^2\ ^3P_2$	218.8389	10	...
Ca XVII +	$2s2p\ ^1P_1^o-2p^2\ ^1S_0$	222.9	55	222.8694	2.6	...
Ca XVII	$2s2p\ ^3P_2^o-2p^2\ ^3P_2$	232.81	80	232.8092	85	...
Ca XVII +	$2s2p\ ^3P_1^o-2p^2\ ^3P_0$	238.4	85	238.3266	22	...
B-like: Ca XVI						
Ca XVI	$2s^22p\ ^2P_{1/2}^o-2s2p^2\ ^2P_{3/2}$	154.8	470	154.8800	186	...
Ca XVI	$2s^22p\ ^2P_{1/2}^o-2s2p^2\ ^2P_{1/2}$	157.9	290	157.7880	123	...
Ca XIII	$2s^22p^4\ ^3P_0-2s2p^5\ ^3P_1^o$	164.22	bl	164.0999	225	...
Ca XVI	$2s^22p\ ^2P_{3/2}^o-2s2p^2\ ^2P_{3/2}$	164.22	1900	164.1660	1000	...
Ca XVI	$2s^22p\ ^2P_{3/2}^o-2s2p^2\ ^2P_{1/2}$	167.42	840	167.4370	412	...
Ca XIV	$2s^22p\ ^2P_{3/2}^o-2s2p^2\ ^2P_{1/2}$	167.42	bl	167.4514	25	...
Ca XVI	$2s^22p\ ^2P_{1/2}^o-2s2p^2\ ^2S_{1/2}$	168.89	860	168.8680	468	...
Ca XVI	$2s^22p\ ^2P_{3/2}^o-2s2p^2\ ^2S_{1/2}$	179.9660	19	...
Ca XVI	$2s^22p\ ^2P_{1/2}^o-2s2p^2\ ^2D_{3/2}$	208.56	785	208.5850	418	...
Ca XV	$2s^22p^2\ ^3P_1-2s2p^3\ ^3D_2^o$...	bl	208.7172	463	...
Ca XVI	$2s^22p\ ^2P_{3/2}^o-2s2p^2\ ^2D_{5/2}$	224.45	700	224.5480	549	...
Ca XVI	$2s^22p\ ^2P_{3/2}^o-2s2p^2\ ^2D_{3/2}$	225.78	38	225.7850	20	...
C-like: Ca XV						
Ca XV	$2s^22p^2\ ^3P_0-2s2p^3\ ^3S_1^o$	137.22 bl	110	137.1954	141	...
Ca XV	$2s^22p^2\ ^3P_1-2s2p^3\ ^3S_1^o$	140.7	400	140.5812	402	140.48
Ca XIV	$2s^22p^3\ ^4S_{3/2}^o-2s2p^4\ ^2D_{3/2}$	140.7	bl	140.6920	1	...
Ca XV	$2s^22p^2\ ^1D_2-2s2p^3\ ^1P_1^o$	141.72	450	141.6865	589	141.69
Ca XV	$2s^22p^2\ ^3P_2-2s2p^3\ ^1D_2^o$	bl	...	144.1390	42	...
Ca XV	$2s^22p^2\ ^3P_2-2s2p^3\ ^3S_1^o$	144.36 bl	550	144.3062	739	...
Ca XV	$2s^22p^2\ ^1D_2-2s2p^3\ ^1D_2^o$	161.1	630	161.0055	1000	...
Ar XII	$2s^22p^3\ ^2D_{3/2}^o-2s2p^4\ ^2S_{1/2}$	bl	...	161.1710	101	...
Ca XIII	$2s^22p^4\ ^3P_2-2s2p^5\ ^3P_2^o$	161.8	790	161.7393	988	161.74
Ca XV	$2s^22p^2\ ^1S_0-2s2p^3\ ^1P_1^o$	162.1	196	162.1453	135	...
Ca XV ?	$2s^22p^2\ ^3P_0-2s2p^3\ ^3P_1^o$	171.5964	131	...
Ca XV ?	$2s^22p^2\ ^3P_1-2s2p^3\ ^3P_2^o$	176.0204	87	...
Ca XV	$2s^22p^2\ ^3P_1-2s2p^3\ ^3P_1^o$	177.1	125	176.9260	211	...
Ca XV ?	$2s^22p^2\ ^3P_1-2s2p^3\ ^3P_0^o$	bl	...	177.2613	162	...
Ca XV	$2s^22p^2\ ^3P_2-2s2p^3\ ^3P_2^o$	181.9	360	181.8996	669	...
Ca XV	$2s^22p^2\ ^3P_2-2s2p^3\ ^3P_1^o$	182.84	110	182.8668	123	...
Ca XV +	$2s^22p^2\ ^3P_0-2s2p^3\ ^3D_1^o$	201.06	454	200.9719	24	...
Ca XV	$2s^22p^2\ ^3P_1-2s2p^3\ ^3D_1^o$	bl	...	208.3216	69	...
Ca XVI	$2s^22p\ ^2P_{1/2}^o-2s2p^2\ ^2D_{3/2}$	208.56	785	208.5850	418	...
Ca XV	$2s^22p^2\ ^3P_1-2s2p^3\ ^3D_2^o$	208.56	bl	208.7172	463	...
Ca XV	$2s^22p^2\ ^3P_2-2s2p^3\ ^3D_3^o$	215.3	440 bl	215.3779	615	...
Ar XII	$2s^22p^3\ ^4S_{3/2}^o-2s2p^4\ ^4P_{1/2}$	215.38	bl	215.4980	320	215.490
Ca XV +	$2s^22p^2\ ^3P_2-2s2p^3\ ^3D_2^o$	217.09	115	217.0350	20.7	...
Ca XV +	$2s^22p^2\ ^1D_2-2s2p^3\ ^3D_3^o$	255.66	140	255.3481	15	...
N-like: Ca XIV						
Ca XIV ?	$2s^22p^3\ ^2D_{3/2}^o-2s2p^4\ ^2P_{1/2}$...	bl ?	128.2556	275	...
Ca XIV +	$2s^22p^3\ ^2D_{3/2}^o-2s2p^4\ ^2P_{3/2}$	132.95	300	132.9160	197	...
Ca XIV	$2s^22p^3\ ^2D_{5/2}^o-2s2p^4\ ^2P_{3/2}$	134.4	600	134.2734	1000	...
Ca XIV	$2s^22p^3\ ^2D_{3/2}^o-2s2p^4\ ^2S_{1/2}$	139.2	120	139.0517	154	...
Ca XIV +	$2s^22p^3\ ^2P_{1/2}^o-2s2p^4\ ^2P_{1/2}$	139.92	1450	140.2100	39	...
Ca XV	$2s^22p^2\ ^3P_1-2s2p^3\ ^3S_1^o$	140.7	400	140.5812	402	140.48
Ca XIV	$2s^22p^3\ ^4S_{3/2}^o-2s2p^4\ ^2D_{3/2}$	140.7	bl	140.6920	1.3	...
Ca XIV	$2s^22p^3\ ^2P_{3/2}^o-2s2p^4\ ^2P_{1/2}$	142.4	175	142.3962	289	...
Ca XIV ?	$2s^22p^3\ ^2P_{1/2}^o-2s2p^4\ ^2P_{3/2}$	145.73	150	145.7986	618	...

Table 1
(Continued)

Spectrum	Transition	Wavelength ^a (Å)	Rel. Int. ^a	Wavelength ^b (Å)	Rel. Int. ^c	Wavelength ^d (Å)
Ca XIV	$2s^2 2p^3 \ ^2P_{3/2}^o - 2s 2p^4 \ ^2P_{3/2}$	148.1	160	148.1640	130	...
Ca XIV	$2s^2 2p^3 \ ^2P_{1/2}^o - 2s 2p^4 \ ^2S_{1/2}$	153.17	175	153.2145	187	...
Ca XIV ?	$2s^2 2p^3 \ ^2P_{3/2}^o - 2s 2p^4 \ ^2S_{1/2}$	155.8288	89	...
Ar XIII	$2s^2 2p^2 \ ^3P_2 - 2s 2p^3 \ ^3S_1^o$	164.8 bl	530	164.8190	650	164.803
Ca XIV +	$2s^2 2p^3 \ ^2D_{3/2}^o - 2s 2p^4 \ ^2D_{5/2}$	164.8 bl	530	164.8625	6	...
Ca XIV	$2s^2 2p^3 \ ^2D_{3/2}^o - 2s 2p^4 \ ^2D_{3/2}$	165.5	bl	165.3455	666	...
Ar X	$2s^2 2p^5 \ ^2P_{3/2}^o - 2s 2p^6 \ ^2S_{1/2}$	165.5	590	166.3655	1000	165.538
Ar XIII	$2s^2 2p^2 \ ^3P_2 - 2s 2p^3 \ ^1D_2^o$	165.5	bl	165.5870	21	...
Ca X	$3d \ ^2D_{3/2} - 4f \ ^2F_{5/2}^o$	166.97	bl	166.9480	701	166.948
Ca XIV	$2s^2 2p^3 \ ^2D_{5/2}^o - 2s 2p^4 \ ^2D_{5/2}$	166.97 bl	500	166.9560	882	...
Ca X	$3d \ ^2D_{5/2} - 4f \ ^2F_{7/2}^o$	166.97	bl	167.0490	1000	167.049
Ca XVI	$2s^2 2p \ ^2P_{3/2}^o - 2s 2p^2 \ ^2P_{1/2}$	167.42	840	167.4370	412	...
Ca XIV	$2s^2 2p^3 \ ^2D_{5/2}^o - 2s 2p^4 \ ^2D_{3/2}$	167.42	bl	167.4514	25	...
Ar XIV	$2s^2 2p \ ^2P_{1/2}^o - 2s 2p^2 \ ^2P_{1/2}$	183.44 bl	340	183.4040	194	183.404
Ca XIV	$2s^2 2p^3 \ ^4S_{3/2}^o - 2s 2p^4 \ ^4P_{1/2}$	183.44 bl	340	183.4603	337	...
Ca XIV +	$2s^2 2p^3 \ ^2P_{1/2}^o - 2s 2p^4 \ ^2D_{3/2}$	185.71	111	185.7641	62	...
Ca XIV +	$2s^2 2p^3 \ ^4S_{3/2}^o - 2s 2p^4 \ ^4P_{3/2}$	186.75	510	186.6103	663	...
Ca XIII	$2s^2 2p^4 \ ^1D_2 - 2s 2p^5 \ ^3P_2^o$	188.77	bl	188.6520	15	...
Ar XI	$2s^2 2p^4 \ ^3P_2 - 2s 2p^5 \ ^3P_2^o$	188.77	280	188.8060	973	188.821
Ca XIV	$2s^2 2p^3 \ ^2P_{3/2}^o - 2s 2p^4 \ ^2D_{5/2}$	188.77	bl	188.9862	157	188.99
Ar XII	$2s^2 2p^3 \ ^2D_{5/2}^o - 2s 2p^4 \ ^2D_{5/2}$	193.63	1040	193.6980	880	193.682
Ca XIV	$2s^2 2p^3 \ ^4S_{3/2}^o - 2s 2p^4 \ ^4P_{5/2}$	193.63	bl	193.8661	967	193.87
Ar XII	$2s^2 2p^3 \ ^2D_{5/2}^o - 2s 2p^4 \ ^2D_{3/2}$	193.9340	35	...
O-like: Ca XIII						
Ca XIII	$2s^2 2p^4 \ ^3P_2 - 2s 2p^5 \ ^1P_1^o$	117.97	100	117.6059	28	...
Ca XIII	$2s^2 2p^4 \ ^1D_2 - 2s 2p^5 \ ^1P_1^o$	131.27	500	131.2172	1000	131.22
Ca XIII ?	$2s^2 2p^4 \ ^1S_0 - 2s 2p^5 \ ^1P_1^o$	148.8808	63	...
Ca XIII	$2s^2 2p^4 \ ^3P_2 - 2s 2p^5 \ ^3P_1^o$	156.74	200	156.6748	353	...
Ca XIII	$2s^2 2p^4 \ ^3P_1 - 2s 2p^5 \ ^3P_0^o$	159.8	110	159.8254	242	...
Ar XIII	$2s^2 2p^2 \ ^3P_1 - 2s 2p^3 \ ^3S_1^o$	161.66	bl	161.6240	365	161.610
Ca XIII	$2s^2 2p^4 \ ^3P_2 - 2s 2p^5 \ ^3P_2^o$	161.8	790	161.7393	988	161.74
Ca XIII	$2s^2 2p^4 \ ^3P_1 - 2s 2p^5 \ ^3P_1^o$	162.98 bl	bl	162.9196	177	...
Ar XIII	$2s^2 2p^2 \ ^1D_2 - 2s 2p^3 \ ^1P_1^o$	162.98	250	162.9800	568	162.957
Ca XIII	$2s^2 2p^4 \ ^3P_0 - 2s 2p^5 \ ^3P_1^o$	164.22	bl	164.0999	225	...
Ca XVI	$2s^2 2p \ ^2P_{3/2}^o - 2s 2p^2 \ ^2P_{3/2}$	164.22	1900	164.1660	1000	...
Ca XIII	$2s^2 2p^4 \ ^3P_1 - 2s 2p^5 \ ^3P_2^o$	168.34	189	168.4029	287	...
Ca XIII +	$2s 2p^5 \ ^1P_1^o - 2p^6 \ ^1S_0$	169.8	94	169.4878	1.6	...
Ca XIII	$2s^2 2p^4 \ ^1D_2 - 2s 2p^5 \ ^3P_2^o$	188.77	bl	188.6520	15	...
Ar XI	$2s^2 2p^4 \ ^3P_2 - 2s 2p^5 \ ^3P_2^o$	188.77	280	188.8060	973	188.821
Ca XIV	$2s^2 2p^3 \ ^2P_{3/2}^o - 2s 2p^4 \ ^2D_{5/2}$	188.77	bl	188.9862	157	188.99
Ca XIII +	$2s^2 2p^4 \ ^1S_0 - 2s 2p^5 \ ^3P_1^o$	217.7	50	217.5589	1.8	...
F-like: Ca XII						
Ca XII	$2s^2 2p^5 \ ^2P_{3/2}^o - 2s 2p^6 \ ^2S_{1/2}$	141.08	1050	141.0412	1000	...
Ca XII	$2s^2 2p^5 \ ^2P_{1/2}^o - 2s 2p^6 \ ^2S_{1/2}$	147.36	300	147.2822	418	...
Ca XII +	$2s^2 2p^4 (^3P) 3s \ ^2P_{3/2}^o - 2s 2p^5 3s (^3P) \ ^2P_{3/2}$	156.35	375	156.2062	1	...
Ne-like: Ca XI						
Ca XI	$2s^2 2p^5 \ 3p \ ^3P_1 - 2s^2 2p^5 \ 4d \ ^3D_2^o$	112.9	bl	112.8210	1.5	...
Ca XI +	$2s^2 2p^5 \ 3p \ ^1D_2 - 2s^2 2p^5 \ 4s \ ^3P_1^o$	135.5	160	135.6280	0.9	...
Ca XI +	$2s^2 2p^5 \ 3d \ ^3F_3 - 2s^2 2p^5 \ 4f \ ^1G_4$	138.2	75	138.0830	0.7	...
Ca XIV	$2s^2 2p^3 \ ^2D_{3/2}^o - 2s 2p^4 \ ^2S_{1/2}$	139.2	120	139.0517	154	...
Ca XI	$2s^2 2p^5 \ 3p \ ^1D_2 - 2s 2p^6 \ 3p \ ^3P_1^o$	139.2	bl	139.1190	0.9	...
Na-like: Ca X						
Ca X +	$3s \ ^2S_{1/2} - 4p \ ^2P_{3/2}^o$	110.95	98	110.9640	9.31	110.963

Table 1
(Continued)

Spectrum	Transition	Wavelength ^a (Å)	Rel. Int. ^a	Wavelength ^b (Å)	Rel. Int. ^c	Wavelength ^d (Å)
Ca X +	$3s^2 S_{1/2} - 4p^2 P_{1/2}^o$	110.95	bl	111.1990	4.60	111.199
Ca X	$3p^2 P_{1/2}^o - 4d^2 D_{3/2}$	122.9890	5	...
Ca X +	$3p^2 P_{3/2}^o - 4d^2 D_{5/2}$	123.7	113 bl	123.7310	10	...
Ca X +	$3p^2 P_{3/2}^o - 4d^2 D_{3/2}$	123.7	113 bl	123.7610	1.1	...
Ca X	$3p^2 P_{1/2}^o - 4s^2 S_{1/2}$	bl	350	151.8440	15	151.843
Ca X	$3p^2 P_{3/2}^o - 4s^2 S_{1/2}$	153.0220	30	153.021
Ca X	$3d^2 D_{3/2} - 4f^2 F_{5/2}^o$	166.97	bl	166.9480	701	166.948
Ca XIV	$2s^2 2p^3^2 D_{5/2}^o - 2s 2p^4^2 D_{5/2}$	166.97	500	166.9560	882	...
Ca X	$3d^2 D_{5/2} - 4f^2 F_{7/2}^o$	166.97	bl	167.0490	1000	167.049
Ca X	$3d^2 D_{5/2} - 4f^2 F_{5/2}^o$	167.0630	50	167.063
Ca X	$3d^2 D_{3/2} - 4p^2 P_{3/2}^o$	206.7510	47	206.75
Ca X	$3d^2 D_{5/2} - 4p^2 P_{3/2}^o$	207.3940	26	207.39
Mg-like: Ca IX						
Ca IX +	$3s^2^1 S_0 - 3s 4p^1 P_1^o$	120.12	140	120.1472	5.3	...
Ca IX +	$3s^2^1 S_0 - 3s 4p^3 P_1^o$	120.6	52	120.5655	2.8	...
Ca IX +	$3s 3p^3 P_1^o - 3s 4s^3 S_1$	162.4	298	162.3738	2.7	162.374
Ca IX	$3s 3p^3 P_3^o - 3s 4s^3 S_1$	bl	bl	163.2314	4.6	163.232
Ca IX +	$3s 3p^1 P_1^o - 3s 4s^1 S_0$	178.56	170	178.5746	26	...
Ar XIII	$2s^2 2p^2^3 P_0 - 2s 2p^3^3 P_1^o$	201.69	81	201.7110	127	201.695
Ca IX +	$3s 3d^1 D_2 - 3s 4f^1 F_3^o$	201.7 bl	60	201.8473	5	...
Al-like: Ca VIII						
Ca VIII	$3s^2 3p^2 P_{1/2}^o - 3s^2 4s^2 S_{1/2}$	182.8	110	182.708
Ca VIII	$3s^2 3p^2 P_{3/2}^o - 3s^2 4s^2 S_{1/2}$	184.2	130	184.157

Notes. The transition identification follows the CHIANTI tables. Observed intensities result from averages but refer to the signal counts registered in a 2 ms exposure; CHIANTI line intensities refer to the strongest line of each spectrum (charge state), which is set to 1000; “+” indicates line intensities much higher than predicted by the CHIANTI model and thus suggesting the likely presence of (unidentified) blends; “?” denotes doubts about the identification a predicted line; bl denotes line blends. Our wavelength values are delimited to reflect the measurement precision of individual lines.

^a This work.

^b From the CHIANTI database v.8 (Del Zanna et al. 2015).

^c From the CHIANTI database v.8 (Del Zanna et al. 2015), but multiplied by 1000 to resemble the experimental signal scale.

^d From the online database at NIST (Kramida et al. 2017).

Relative line intensities are important for line identification purposes. However, the production of a given charge state depends on the electron temperature, which in the discharge may vary with time and location in the plasma. Hence our spectra are not governed by a single temperature value, and line ratios are expected to be valid only for a given charge state. We further neglect a number of technical details of the impurity transport and viewing geometry in the given apparatus, which we consider as secondary in the present context. Despite combining every 10 sequential spectra (20 ms), the significant variations with the occurrence of the laser injections survive this smoothing procedure. We find only slight variations of relative line intensities for a given ion species.

The overall spectral response function of the spectrograph and detector is expected to be smooth and the detection efficiency decreasing toward long wavelengths, as has been demonstrated for a sister instrument (Lepson et al. 2016). Our observed line intensities have not been corrected for this overall trend; within a given line multiplet the effect is expected to be moderate. For the aforementioned sister instrument and observations near 200 Å the trend would imply a change in detection efficiency by about a factor of two over a wavelength interval of about 40 Å. We do

not see such a systematic variation of the relative signal seen versus predicted by CHIANTI in our present data.

Our timescale within the discharge time is very long in comparison to almost all the atomic level lifetimes. Therefore, the time history we observe reflects the excitation conditions in the time-varying plasma rather than atomic properties. This leaves mainly the wavelengths to assess likely identifications of unknown lines, plus the plasma discharge phases. In practice, many of the apparent wavelengths vary slightly during the discharge, because the line blends change in composition. Incidental line blends affect the apparent wavelengths most strongly in the early discharge phases, whereas later in the same discharge, when the blending contributions from contaminants are lower, many of the wavelengths approximate the literature values of known lines.

In many cases the relative line intensities of our data are compatible to the CHIANTI model predictions, while in others there are gross mismatches. Some of these line intensity mismatches may be due to blends with unidentified lines, while others may eventually be tracked to shortcomings of the model. Where the observed intensity is much higher than projected, often suggesting the presence of an unidentified line, we have added a “+?” mark to the spectrum identifier; where a

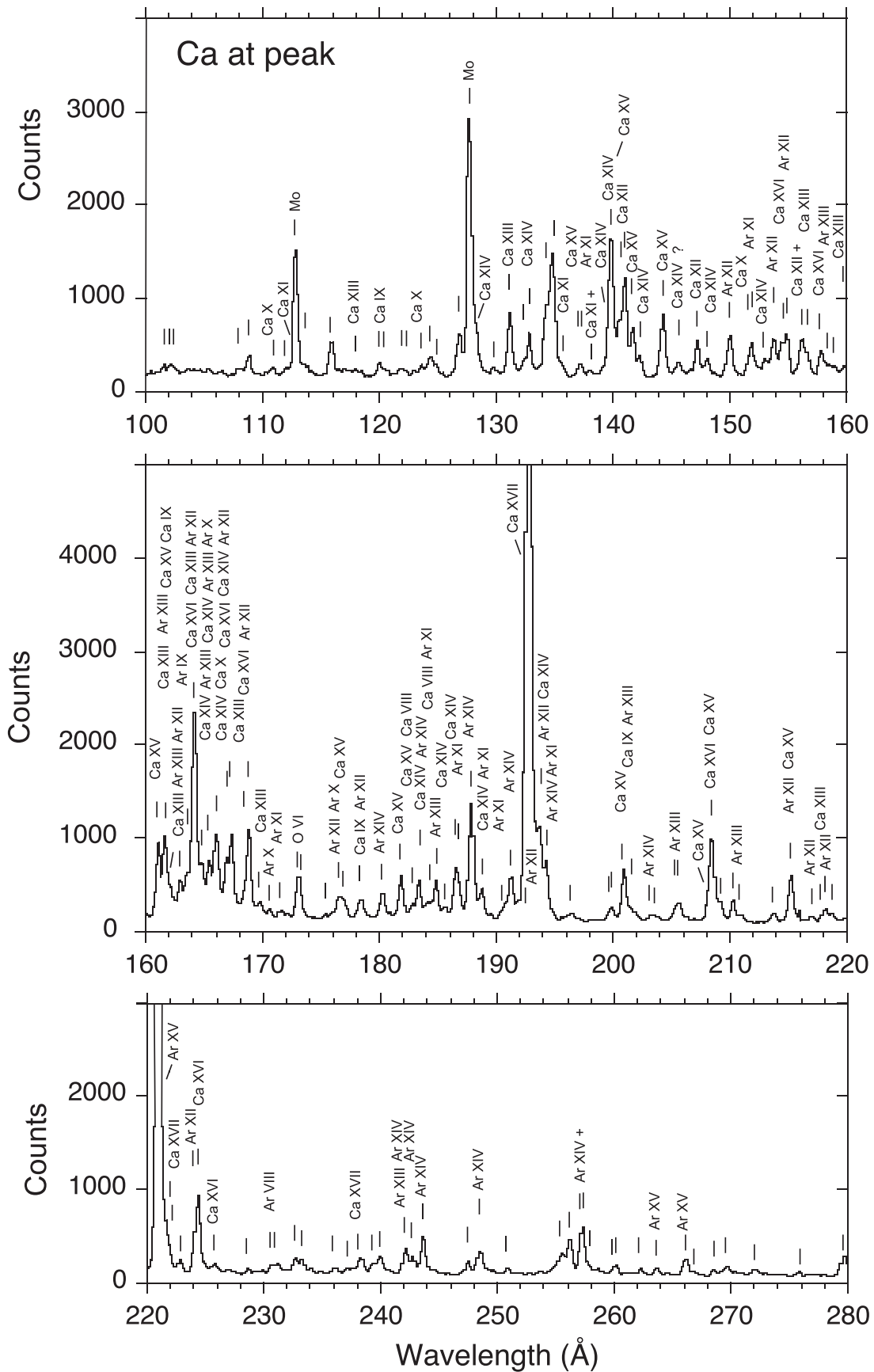


Figure 3. Detail spectra during CaF₂ laser ablation (peak Ca signal). Recognized peaks are indicated by fiducial markers. Lines identified with Ca or Ar are marked by the spectrum number; for details, see Table 1.

Table 2Ar Lines Observed in the Wavelength Band $\lambda 100$ to $\lambda 285$ in the Injection Phase of the Tokamak Plasma, but Just before the Actual Injection of CaF₂ (See the Text)

Spectrum	Transition	Wavelength ^a (Å)	Rel. Int. ^a	Wavelength ^b (Å)	Wavelength ^c (Å)	Rel. Int. ^d	Wavelength ^e (Å)
Be-like: Ar XV							
Ar XV	$2s^2 \ ^1S_0-2s2p \ ^1P_0^o$	221.05	5200	...	221.1356	1000	...
Ar XV	$2s2p \ ^3P_0^o-2p^2 \ ^3P_1$	258.7635	12	...
Ar XV	$2s2p \ ^3P_1^o-2p^2 \ ^3P_1$	263.7	130	...	263.6684	9	...
Ar XV	$2s2p \ ^3P_2^o-2p^2 \ ^3P_2$	266.24	200	...	266.2348	37	...
B-like: Ar XIV							
Ar XIV	$2s^22p \ ^2P_{1/2}^o-2s2p^2 \ ^2P_{3/2}$	180.26	240	...	180.2850	191	...
Ar XIV	$2s^22p \ ^2P_{1/2}^o-2s2p^2 \ ^2P_{1/2}$	183.44 bl	340	183.39	183.4040	194	183.404
Ar XIV	$2s^22p \ ^2P_{3/2}^o-2s2p^2 \ ^2P_{3/2}$	187.96	1140	187.977	187.9620	1000	187.962
Ar XIV	$2s^22p \ ^2P_{3/2}^o-2s2p^2 \ ^2P_{1/2}$	191.36	420	191.38	191.3550	376	191.355
Ar XIV	$2s^22p \ ^2P_{1/2}^o-2s2p^2 \ ^2S_{1/2}$	194.27	635	194.38	194.4010	400	194.401
Ar XIV	$2s^22p \ ^2P_{3/2}^o-2s2p^2 \ ^2S_{1/2}$	203.31	140	203.34	203.3580	58	203.358
Ar XIV	$2s^22p \ ^2P_{1/2}^o-2s2p^2 \ ^2D_{3/2}$	243.75	320	...	243.7510	399	...
Ar XIV	$2s^22p \ ^2P_{3/2}^o-2s2p^2 \ ^2D_{5/2}$	257.38	460	...	257.3680	562	...
Ar XIV	$2s^22p \ ^2P_{3/2}^o-2s2p^2 \ ^2D_{3/2}$	257.9990	31	...
C-like: Ar XIII							
Ar XIII	$2s^22p^2 \ ^3P_0-2s2p^3 \ ^3S_1^o$	159.1	150	...	159.0890	126	159.077
Ar XIII	$2s^22p^2 \ ^3P_1-2s2p^3 \ ^3S_1^o$	161.66	bl	...	161.6240	365	161.610
Ar XIII	$2s^22p^2 \ ^1D_2-2s2p^3 \ ^1P_1^o$	162.98	250	...	162.9800	568	162.957
Ar XIII	$2s^22p^2 \ ^3P_2-2s2p^3 \ ^3S_1^o$	164.8	530	...	164.8190	650	164.803
Ar X	$2s^22p^5 \ ^2P_{3/2}^o-2s2p^6 \ ^2S_{1/2}$	165.5	590 bl	165.548	166.3655	1000	165.538
Ar XIII	$2s^22p^2 \ ^3P_2-2s2p^3 \ ^1D_2^o$	165.5	bl	...	165.5870	21	...
Ar XI	$2s^22p^4 \ ^3P_2-2s2p^5 \ ^3P_1^o$	184.51	184.5240	342	184.511
Ar XIII	$2s^22p^2 \ ^1D_2-2s2p^3 \ ^1D_2^o$	184.9	375	184.91	184.9330	1000	184.900
Ar XIII	$2s^22p^2 \ ^1S_0-2s2p^3 \ ^1P_1^o$...	bl	186.39	186.4140	133	186.382
Ar XIII	$2s^22p^2 \ ^3P_0-2s2p^3 \ ^3P_1^o$	201.69	81	201.69	201.7110	127	201.695
Ar XIII	$2s^22p^2 \ ^3P_1-2s2p^3 \ ^3P_2^o$	205.2	50	205.263	205.2870	104	205.254
Ar XIII	$2s^22p^2 \ ^3P_1-2s2p^3 \ ^3P_1^o$	205.67	145	205.776	205.8040	166	205.784
Ar XIII	$2s^22p^2 \ ^3P_1-2s2p^3 \ ^3P_0^o$	205.922	205.9500	145	205.940
Ar XIII	$2s^22p^2 \ ^3P_2-2s2p^3 \ ^3P_2^o$	210.42	170	210.453	210.4680	583	210.432
Ar XIII	$2s^22p^2 \ ^3P_2-2s2p^3 \ ^3P_1^o$	211.1	50	210.994	211.0110	136	210.989
Ar XIII	$2s^22p^2 \ ^3P_0-2s2p^3 \ ^3D_1^o$	236.2	100	...	236.2850	196	...
Ar XIII	$2s^22p^2 \ ^3P_1-2s2p^3 \ ^3D_1^o$...	bl	...	241.9210	76	...
Ar XIII	$2s^22p^2 \ ^3P_1-2s2p^3 \ ^3D_2^o$	242.22	190	...	242.2400	406	...
Ar XIII +	$2s^22p^2 \ ^1D_2-2s2p^3 \ ^3P_2^o$	242.9	90	...	242.7440	0.9	...
Ar XIII	$2s^22p^2 \ ^3P_2-2s2p^3 \ ^3D_3^o$	248.64	180	...	248.6970	562	...
Ar XIII	$2s^22p^2 \ ^3P_2-2s2p^3 \ ^3D_2^o$	249.4870	35	...
N-like: Ar XII							
Ar XII ?	$2s^22p^3 \ ^2D_{3/2}^o-2s2p^4 \ ^2P_{1/2}$	149.9290	353	...
Ar XII	$2s^22p^3 \ ^2D_{3/2}^o-2s2p^4 \ ^2P_{3/2}$	153.8 bl	400	...	153.6280	186	...
Ar XII	$2s^22p^3 \ ^2D_{5/2}^o-2s2p^4 \ ^2P_{3/2}$	154.5	480	...	154.4220	1000	...
Ar XII ?	$2s^22p^3 \ ^2D_{3/2}^o-2s2p^4 \ ^2S_{1/2}$	161.1710	101	...
Ar XII +	$2s^22p^3 \ ^2P_{1/2}^o-2s2p^4 \ ^2P_{1/2}$	163.27	440	...	163.2330	52	...
Ar XII ?	$2s^22p^3 \ ^2P_{3/2}^o-2s2p^4 \ ^2P_{1/2}$	bl	164.5420	235	...
Ar XII ?	$2s^22p^3 \ ^2P_{1/2}^o-2s2p^4 \ ^2P_{3/2}$	167.6270	57	167.623
Ar XII ?	$2s^22p^3 \ ^2P_{3/2}^o-2s2p^4 \ ^2P_{3/2}$	169.01	30	...	169.0080	154	169.004
Ar XII	$2s^22p^3 \ ^2P_{1/2}^o-2s2p^4 \ ^2S_{1/2}$	176.67 bl	150	...	176.6470	177	...
Ar XII	$2s^22p^3 \ ^2P_{3/2}^o-2s2p^4 \ ^2S_{1/2}$	178.2	178.1810	137	...
Ar XII	$2s^22p^3 \ ^2D_{3/2}^o-2s2p^4 \ ^2D_{5/2}$	bl	192.4500	14	...
Ar XII ?	$2s^22p^3 \ ^2D_{3/2}^o-2s2p^4 \ ^2D_{3/2}$	192.58 bl	35	192.67	192.6830	640	192.675
Ar XII	$2s^22p^3 \ ^2D_{5/2}^o-2s2p^4 \ ^2D_{5/2}$	193.63	1040	193.68	193.6980	880	193.682
Ar XII	$2s^22p^3 \ ^2D_{5/2}^o-2s2p^4 \ ^2D_{3/2}$	bl	193.9340	35	...
Ar XI ?	$2s^22p^4 \ ^3P_1-2s2p^5 \ ^3P_2^o$	bl	...	194.06	194.1040	294	194.118
Ar XII	$2s^22p^3 \ ^2P_{1/2}^o-2s2p^4 \ ^2D_{3/2}$...	bl	215.233	215.2260	65	...

Table 2
(Continued)

Spectrum	Transition	Wavelength ^a (Å)	Rel. Int. ^a	Wavelength ^b (Å)	Wavelength ^c (Å)	Rel. Int. ^d	Wavelength ^e (Å)
Ar XII	$2s^2 2p^3 \ ^4S_{3/2} - 2s 2p^4 \ ^4P_{1/2}$	215.38	440	215.498	215.4980	320	215.490
Ar XII	$2s^2 2p^3 \ ^2P_{3/2} - 2s 2p^4 \ ^2D_{5/2}$	bl	...	217.22	217.2120	156	217.200
Ar XII	$2s^2 2p^3 \ ^4S_{3/2} - 2s 2p^4 \ ^4P_{3/2}$	218.27	110	...	218.2930	630	218.290
Ar XII	$2s^2 2p^3 \ ^4S_{3/2} - 2s 2p^4 \ ^4P_{5/2}$	224.2	290	...	224.2500	924	...
O-like: Ar XI							
Ar XI +	$2s^2 2p^4 \ ^3P_2 - 2s 2p^5 \ ^1P_1^o$	137.22 bl	110	...	136.9180	16	...
Ar IX +	$2s^2 2p^5 \ 3s \ ^3P_2^o - 2s 2p^5 \ 4p \ ^3S_1$	137.22 bl	110	...	137.2420	1	...
Ar XI	$2s^2 2p^4 \ ^1D_2 - 2s 2p^5 \ ^1P_1^o$	151.91	350	...	151.8540	1000	...
Ar XI ?	$2s^2 2p^4 \ ^1S_0 - 2s 2p^5 \ ^1P_1^o$	171.89	171.8660	62	171.862
Ar XI ?	$2s^2 2p^4 \ ^3P_2 - 2s 2p^5 \ ^3P_1^o$	184.51	184.5240	342	184.511
Ar XI ?	$2s^2 2p^4 \ ^3P_1 - 2s 2p^5 \ ^3P_0^o$	187.09	187.0900	249	187.080
Ar XI	$2s^2 2p^4 \ ^3P_2 - 2s 2p^5 \ ^3P_2^o$	188.77	280	188.83	188.8060	973	188.821
Ar XI	$2s^2 2p^4 \ ^3P_1 - 2s 2p^5 \ ^3P_1^o$	189.58	...	189.60	189.5800	182	189.566
Ar XI	$2s^2 2p^4 \ ^3P_0 - 2s 2p^5 \ ^3P_1^o$	190.8	112	190.98	190.9750	233	190.96
Ar XI	$2s^2 2p^4 \ ^3P_1 - 2s 2p^5 \ ^3P_2^o$	bl	...	194.06	194.1040	294	194.118
F-like: Ar X							
Ar X	$2s^2 2p^5 \ ^2P_{3/2}^o - 2s 2p^6 \ ^2S_{1/2}$	165.5	590	165.548	166.3655	1000	165.538
Ar X	$2s^2 2p^5 \ ^2P_{1/2}^o - 2s 2p^6 \ ^2S_{1/2}$	170.64	90	170.642	171.5204	440	170.642
Ar X	$2s^2 2p^4 \ (^3P) 3s \ ^2P_{3/2}^o - 2s 2p^5 \ 3s \ (^3P) \ ^2P_{1/2}$	bl	176.8413	0.3	...
Ne-like: Ar IX							
Ar IX +	$2s^2 2p^5 3p \ ^3D_2 - 2s 2p^6 3p \ ^3P_1^o$	163.58	318	...	163.6350	0.5	...
Na-like: Ar VIII							
Ar VIII	$3p \ ^2P_{1/2}^o - 4s \ ^2S_{1/2}$	229.4300	11	...
Ar VIII	$3p \ ^2P_{3/2}^o - 4s \ ^2S_{1/2}$	230.8	20	...	230.8670	21	...
Mg-like: Ar VII							
Ar VII	$3s^2 \ ^1S_0 - 3s 4p \ ^1P_1^o$	175.6	...	175.52	175.501
Ar VII	$3s 3p \ ^1P_1^o - 3s 4s \ ^1S_0$	279.1890	17	...

Notes. The transition identification follows the CHIANTI tables. Observed intensities result from averages but refer to the signal counts registered in a 2 ms exposure; CHIANTI line intensities refer to the strongest line of each spectrum (charge state), which is set to 1000; “+” indicates line intensities much higher than predicted by the CHIANTI model and thus suggests the likely presence of (unidentified) blends; “?” denotes doubts about the identification of a predicted line; bl denotes line blends. Our wavelength values are delimited to reflect the measurement precision of individual lines.

^a This work.

^b From higher-resolution work at the Livermore EBIT (Beiersdorfer et al. 2014b; Träbert et al. 2014b; Beiersdorfer & Träbert 2017).

^c From the CHIANTI database v.8 (Del Zanna et al. 2015).

^d From the CHIANTI database v.8 (Del Zanna et al. 2015), but multiplied by 1000 to resemble the experimental signal scale.

^e From the online database at NIST (Kramida et al. 2017).

predicted line seems to be missing, we add a “?” for the doubtful identity.

3.1. F

Fluorine must be present in our laboratory light source, as it is part of the material (CaF₂) that is used for the (proven) injection of Ca into the plasma. Kelly (1987) lists several hundred lines of F V to F VIII in the EUV wavelength range. However, many of these lines belong to transitions in which the lower level is excited, which are not easily produced under (relatively) low-density conditions. A few lines with wavelengths close to fluorine literature data appear in the first phase of the discharge, which means before injection, thus ruling out their identification with F.

3.2. Ca

Ca is present only after laser injection (Figures 2 and 3). Thus, spectral lines observed in the early spectra serve as a veto against identification with Ca, but may indicate a (later) line blend. At several wavelengths listed by CHIANTI for Ca, the signal curve shows the appropriate wiggles in sync with the laser injections (Figure 5), yet spectra in the middle of the discharge do not show spectral lines in these positions. In Table 1, we associate only those lines with Ca that show a significant signal during the laser injection phase.

The strongest lines seen in the spectra of this discharge phase are the $3s^2 \ ^1S_0 - 3s 3p \ ^1P_1^o$ resonance lines of Be-like Ar XV and Ca XVII. These two lines are of almost the same signal strength (see Figure 2). The temporal evolution of the Ca XVII line is shown in Figure 5(b). Here the signal amplitude during injection

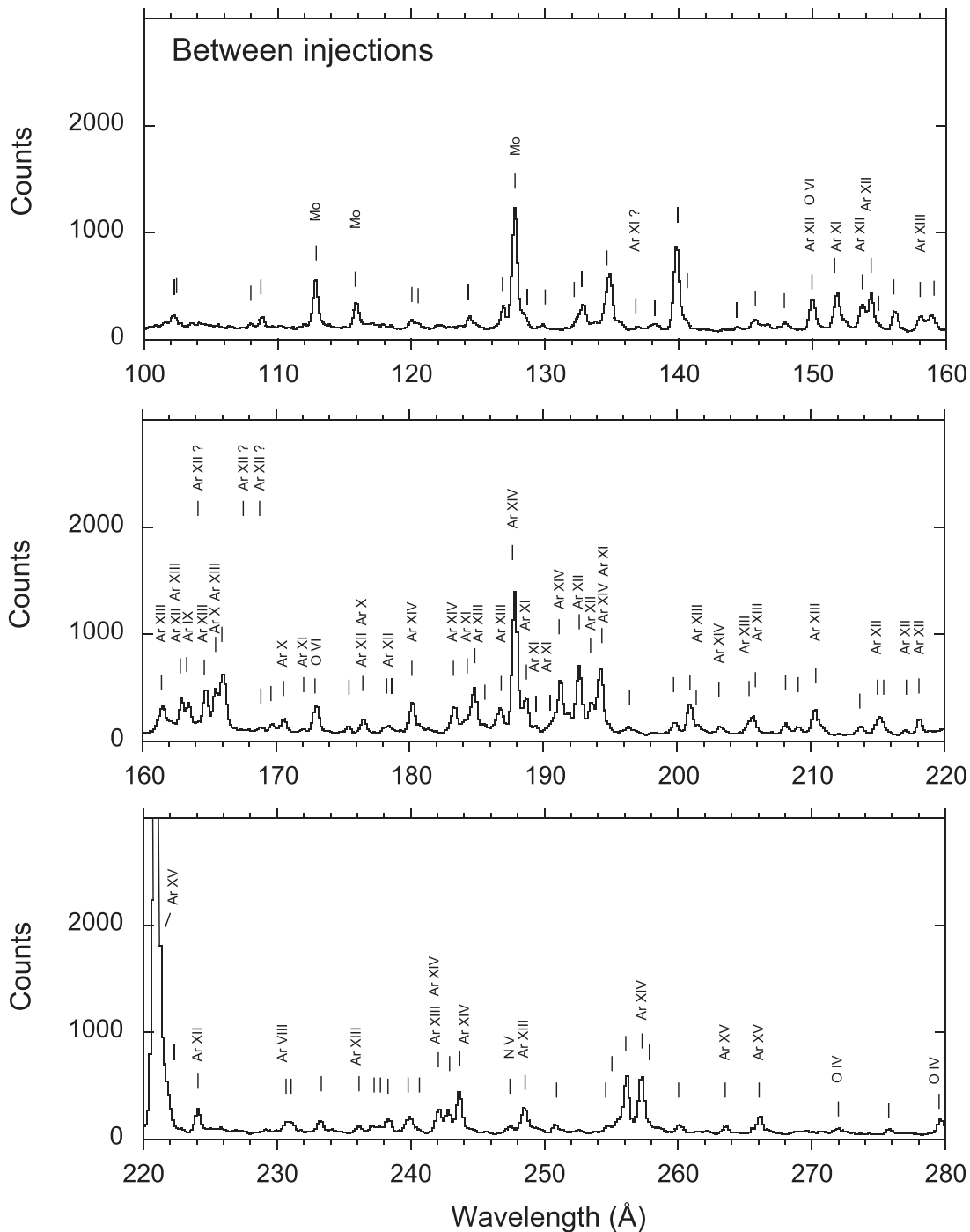


Figure 4. Detail spectra just before CaF_2 laser ablation (Ca signal is absent). Recognized peaks are indicated by fiducial markers. Lines identified as Ar (and a few light elements) are marked by the spectrum number; for details, see Table 2.

even exceeds the non-Ca light level in the start-up phase. However, the signal at injection sits on top of a sizeable plateau composed of plasma radiation without elemental identification. A fair number of lines associated with Ca in the literature are mentioned in Table 1. As mentioned, we consider a corroboration successful only if the line is seen in the spectra in the middle phase of the discharge, with laser injection. Where this criterion fails, the spectrum identifier is earmarked with a question mark. There also are lines that previously were not identified with Ca, but appear at the right time of the discharge. Here the marker is the chemical element symbol plus a question mark. Unfortunately, several of the Ca lines listed by Kelly (1987; and largely adopted

by CHIANTI) are blended with Ar lines or lines of uncertain identity. Moreover, the CHIANTI model computations comprise very many lines, but most of these are not expected to be sufficiently prominent under our measurement conditions. This also applies to the multitude of lines derived from the CHIANTI model without any experimental confirmation (their starred notation), and that practically all remain unseen.

In order to exploit the relative line intensities for testing and future use in spectrum analysis, we list relative line intensities averaged from the maxima of the first or second laser pulse, as well as predicted CHIANTI line intensities in Table 1. The CHIANTI line intensities are normalized to a value of 1 for

Table 3
Lines Observed in the Wavelength Band $\lambda 100$ to $\lambda 285$ in the Laser Injection Phase of the Tokamak Plasma

Spectrum	Transition	Wavelength ^a (Å)	Rel. Int. ^a	Wavelength ^b (Å)	Rel. Int. ^c	Wavelength ^d (Å)
Ca ?	...	101.64	106
Ca ?	...	102.28	160
Ca ?	...	104.47	100
Mo XXXIV	$2s^2 2p^5 \ ^2P^o \ J = 3/2-1/2 \ (M1)$	112.9 bl	1200	112.828
F, Ca	...	113.7	130
Mo XXXI	$3s^2 \ ^1S_0-3s3p \ ^1P^o$	115.96	310	115.999
Ca ?	...	117.9	196
Ca ?	...	118.6	57
F, Ca ?	...	122.1	80
F, Ca, Mo ?	...	124.4	170
F, Ca, Mo IX ?	...	124.93	117	124.914
Mo XXXII	$3s \ ^2S_{1/2}-3p \ ^2P^o_{3/2}$	127.86	2100	127.868
O, F, Ar, Ca ?	...	128.45	400
O, F, Ca ?	...	129.9 bl	74
O, Ca ?	...	132.5	150
Ar ?	...	134.4 bl	700
F, Ar ?	...	134.85 bl	1200
F, Ca, Mo ?	...	135.5	160
F, Ca, Mo ?	...	146.7	100
F, Ca ? ?	...	158.12	194
Ca ?	...	158.6	164
F v ? + Ca ?	...	166.16	820	166.18
O VI	$2p-3d$	173.1 bl	410	...	172.9357	...
O VI	$2p-3d$	173.1	410	...	173.0798	...
Ca ?	...	196.4	100
Ca ?	...	199.96	82
F v	205.55
N v, Ca ?	...	209.13	130	209.275
O IV, Ar?	$2s-3p$	213.85	140	213.6620
Ca ?	...	216.1	140
Ar ?	...	221.75	480
Ca ?	...	231.1	75
O v, Ca?	...	233.4	80	233.451
F, Ca ?	...	239.5	38
F, Ca ?	...	240.0	110
Ca ?	...	250.9	120
He II	$1s \ ^2S_{1/2}-3p \ ^2P^o_{1/2,3/2}$	256.3	320	...	256.317	...
Ar, Ca?	...	260.1	120
O IV, Ar ?	...	279.8	140
Ar ?	...	281.9	100

Notes. Unidentified likely blends of the lines in Tables 1 and 2 are not repeated here. Line intensities refer to the scale of Table 1. Literature wavelengths are listed of lines of N, O, F, Ar, Ca, and Mo that might plausibly appear here. Tentative elemental identifications (elements with a question mark) are based on the appearance during (F, Ca) injection (see the text). bl denotes line blends.

^a This work.

^b From the CHIANTI database v.8 (Del Zanna et al. 2015).

^c From the CHIANTI database v.8 (Del Zanna et al. 2015), but multiplied by 1000 to resemble the experimental signal scale.

^d From the online database at NIST (Kramida et al. 2017).

the strongest EUV line of a given spectrum. The temperature assumed is that for the maximum production of each charge state, which in a machine like Alcator also relates to a different location in the plasma. We multiply these values by a factor of 1000 to obtain numbers closer to the ballpark of our experimental scale. The experimental line intensities have not been corrected for the (unknown) responsivity as a function of wavelength of the spectrometer. For the comparison, we use the CHIANTI model intensities that refer to an electron density of $n_e = 10^{15} \text{ cm}^{-3}$, close to the electron density $n_e \approx 10^{14} \text{ cm}^{-3}$ in Alcator. Table 1 lists known lines of calcium that fall into the spectral range of this experiment sorted by spectrum number.

Weak lines are included in the presentation only if their predicted intensity exceeds about 1% of the strongest line of a given spectrum, or if a stronger line appears in the spectrum than is warranted by the CHIANTI model.

3.2.1. Be-like: Ca XVII

In Ca XVII, the resonance transition $2s^2 \ ^1S_0-2s2p \ ^1P^o$ at 192.83 \AA stands out. This line has been discussed in plasma physics detailed before by Rice et al. (2007). The measured signal (about 7000) is a factor of seven higher than the arbitrarily chosen value 1000 from the model computation. CHIANTI provides model estimates of the next strongest lines

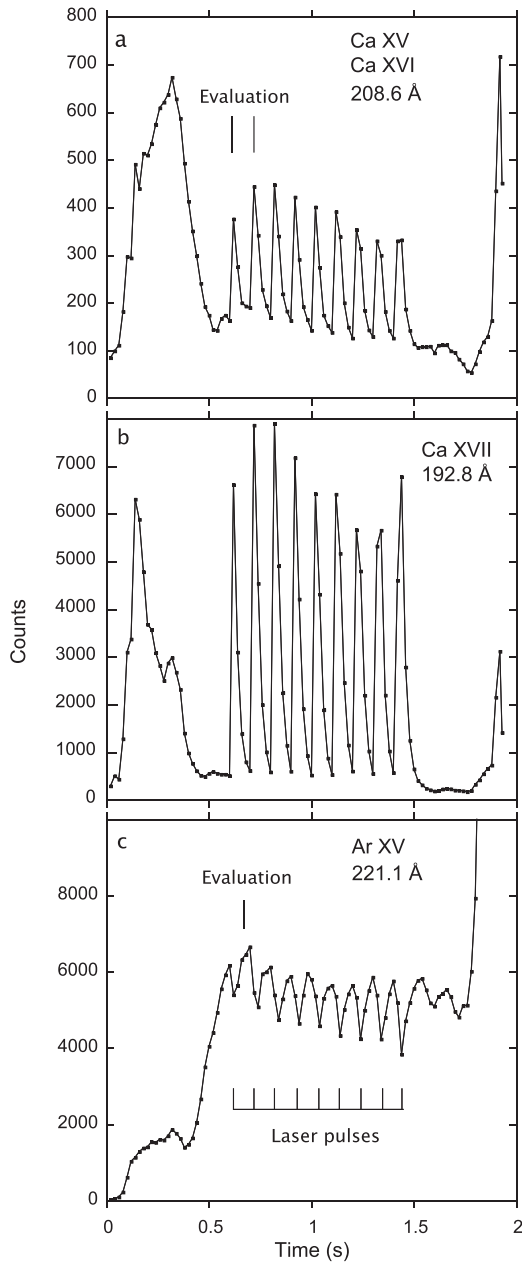


Figure 5. Time traces at the wavelengths of selected Ca and Ar lines. (a) Ca XV and Ca XVI $\lambda 208.5 \text{ \AA}$, (b) Ca XVII resonance line $\lambda 192.85$, and (c) Ar XV resonance line $\lambda 221.1356 \text{ \AA}$. The Ar signal shows a dip at each laser pulse (CaF₂ injection). The evaluation of the Ca line intensities (Table 1) refers to the average of the first two laser injection peaks (as marked in panel a), whereas the evaluation of the Ar line intensities (Table 2) refers to the interval between the first two injections (marked in panel c).

(line intensities ranging from about three to 85), which all are from $2s2p-2p^2$ transitions. At wavelengths commensurate with the known level structure, we seem to see three of the four lines in our wavelength range. However, their relative intensities do not match the intensity factor seen with the resonance line. For example, from basic principles, the strongest line of the $2s2p\ ^3P^o_j-2p^2\ ^3P^o_j$ multiplet ($\lambda 232.8$) originates from the $J = 2-J' = 2$ transition; here model and measurement (with their somewhat arbitrary scales) yield about the same numerical value of 80. Thus the line is about a factor of 7 weaker than predicted by the CHIANTI model (by reference to the resonance transition). The intensities of the other lines of the

same multiplet do not match any such comparison. For example, we see a line at 222.9 \AA with a signal of “55,” that is practically identical to the CHIANTI listing of 222.8694 \AA ; however, CHIANTI predicts the line with an intensity of “2.6.” Consequently, the signal of the $\lambda 222.9$ line, small as it is, is likely due to another as yet unidentified transition.

3.2.2. B-like: Ca XVI

The dynamic range of the strongest transitions is much more favorable for our observations of Ca XVI than for Ca XVII. Table 1 lists nine lines of this spectrum, all from $2s-2p$ transitions. The signal of the strongest line, $2s^22p\ ^2P^o_{3/2}-2s2p^2\ ^2P^o_{3/2}$ at 164.22 \AA , exceeds the arbitrary reference value from CHIANTI by about a factor of two (in part due to a blend with Ca XIII), and the same factor roughly describes the other lines as well. The $\lambda 154.8$ line exceeds this relation somewhat, and the $\lambda 224.45$ line falls somewhat short of the CHIANTI expectation. The much weaker $\lambda 167.45$ line is blended with its stronger neighbor of the same spectrum.

3.2.3. C-like: Ca XV

Ca XV is particularly rich in lines in our spectral range. The strongest line, $2s^22p^2\ ^1D_2-2s2p^3\ ^1D_2^o$ at $\lambda 161.1$, has a signal that amounts to 0.6 of the (arbitrarily normalized) CHIANTI model prediction. Many of the other Ca XV lines fit to a line intensity pattern reasonably close to the CHIANTI model one. The $\lambda 140.7$ line is stronger than predicted, and the blend with the nearby weak Ca XIV $\lambda 140.69$ line does not explain the difference sufficiently. Several predicted and reasonably strong Ca XV lines ($\lambda 171.6$, $\lambda 176.0$, $\lambda 208.3$, $\lambda 208.7$) are not detected, the line at $\lambda 177.3$ is possibly blended with a neighbor (at $\lambda 176.9$), and the $\lambda 215.4$ line appears to be blended with the Ar XII $\lambda 215.5$ line. The two longest wavelength Ca XV lines of our sample should be weak. The stronger lines appearing near their locations are thus likely of another origin.

3.2.4. N-like: Ca XIV

The factor between our measurement signal and the (scaled) CHIANTI model prediction for the strongest Ca XIV line $2s^22p^3\ ^2D^o_{5/2}-2s2p^4\ ^2P^o_{3/2}$ at $\lambda 134.4$ is about 0.6. However, for the other lines assumed to belong to this spectrum, the scatter of the ratio of signal and model is considerable. For example, the predicted $\lambda 128.3$ line is not resolved, the CHIANTI line $\lambda 145.8$ appears at about half the expected signal, while at the position $\lambda 140.2$, $\lambda 164.9$, $\lambda 167.4$, and $\lambda 185.7$ lines appear that are much stronger (up to a factor of 60 or more) than the expected Ca XIV lines. We therefore assume that these lines we see are not Ca XIV lines. At $\lambda 165.5$, there is a triple line blend, with a weak Ar XIII line and a strong Ar X line. The $\lambda 165.3455$ line (according to CHIANTI) should be partly resolved from the Ar X line, but is at most causing a slight wavelength shift of the blended spectral feature. If the line was anywhere nearly as strong as predicted by the CHIANTI model the effect should be more notable. At $\lambda 164.8625$, CHIANTI predicts a weak line, but a much stronger one (by two orders of magnitude) is seen. There also are notable differences in wavelength between the Kelly (1987) tables and CHIANTI. These findings suggest that these lines need a reinvestigation at higher spectral resolution, especially since we find a large disconnect between the measured and calculated line intensities, which could indicate that the CHIANTI Ca XIV model is in part at fault.

3.2.5. O-like: Ca XIII

The factor between our signal and the scaled CHIANTI model prediction for the strongest Ca XIII line $2s^2 2p^4 \ ^1D_2-2s2p^5 \ ^1P_1$ at $\lambda 131.2$ is about 0.5. Several lines are seen at line intensities roughly commensurate with this ratio. A few lines predicted to be relatively weak are not seen, while at the positions of another few predicted weak lines we see clearly more intense lines, which may indicate other origins.

3.2.6. F-like: Ca XII

Three lines, in principle, are associated with Ca XII. Two of these $2s^2 2p^5 \ ^2P_{3/2,1/2}-2s2p^6 \ ^2S_{1/2}$ at $\lambda 141.08$ and $\lambda 147.36$, respectively, roughly fit the expected line intensity pattern. The third line, $\lambda 156.3$, is two orders of magnitude stronger than the model predicts and thus must belong to another ion species.

3.2.7. Ne-like: Ca XI

The strongest Ca XI line of the CHIANTI model is not inside our working range, and consequently there is no valid conversion factor available for the model line intensities and the observed signal. However, all four Ca XI lines in our wavelength range are predicted to be very weak (the lower level is not in the ground configuration). The moderately strong lines we observe thus must have other origins, which in only one case is known (Ca XIV).

3.2.8. Na-like: Ca X

For Ca X, the CHIANTI model predicts mostly weak lines in our wavelength range. An exception are two of the Ca X 3d–4f transitions ($\lambda 166.95$, $\lambda 167.05$), for which experience with low-density plasmas does not let us expect much signal, because the lower level is not in the ground configuration. Unfortunately, the two lines are not only not resolved from each other in our spectra, but they are blended with a Ca XIV line at $\lambda 166.96$. Thus they cannot be seen properly with our experimental setup.

3.2.9. Mg-like: Ca IX

For Ca IX, the CHIANTI model predicts mostly weak lines in our wavelength range. We observe much stronger lines near the given wavelengths, and the line intensity pattern does not resemble the model. In one case, the blend can be identified with an Ar XIII line, whereas for the other four line positions, line blends dominated by foreign lines have to be assumed.

3.2.10. Al-like: Ca VIII

For Ca VIII in our wavelength interval, CHIANTI does not expect any lines. The NIST ASD database names the two $3s^2 \ 3p \ ^2P_{1/2,3/2}-3s^2 \ 4s \ ^2S_{1/2}$ lines, which in this system are from ground-state transitions. The observed line intensities are roughly consistent with such transitions.

3.3. Ar

Ar is present throughout the duration of the plasma discharge, and overall the signal rises during the discharge (Figure 5(c)). However, the time history differs drastically from that of Ca (Figures 5(a), (b)) in that there are minima in the signal that coincide with the laser injection events. Our Ar data evaluation mainly refers to data obtained in a 10 ms interval between laser injections (which are spaced by about 50 ms),

just before the second CaF₂ injection. At this time there is no apparent Ca contribution seen in the spectra, and therefore the spectrum (Figure 4) can be analyzed and discussed without having to deal with blends of Ar lines with those of Ca. For reasons of statistical reliability, some of the Ar line intensities in Table 2 have, however, been averaged over several spectra; these averages include spectra taken in other 10 ms time slots during the discharge, some of which may contain some signal of Ca (although the data have been taken near Ca minima). For the Ar line ratios of interest, no significant variation was observed among the time slots.

A number of Ar lines have been observed in high-resolution studies at the Livermore electron beam ion trap (Beiersdorfer et al. 2014b; Träbert et al. 2014a, 2014b; Beiersdorfer & Träbert 2017), where numerous data have been compared to the listings in the NIST and CHIANTI databases. Not all Ar lines listed by CHIANTI are corroborated by those data. For example, the compilers of the CHIANTI database have erred in not adopting the Kelly wavelengths (Kelly 1987) of the principal lines of Ar X (see Beiersdorfer & Träbert 2017). This error is noticeable also in our present measurement, even though observed with lower resolving power than these other argon measurements. A few new lines have a time history during the discharge that resembles that of well established Ar lines; in Table 2, these lines are denoted by the elemental symbol with a question mark, since we cannot offer full identifications.

3.3.1. Be-like: Ar XV

For the $2s^2 \ ^1S_0-2s2p \ ^1P_1^o$ resonance line of Ar XV, the ratio between the signal and the arbitrarily scaled CHIANTI model line intensity is about five. Three of the $2s2p \ ^3P_j^o-2p^2 \ ^3P_j'$ transitions are expected to yield lines in our operating wavelength range. One of the latter agrees with the conversion factor, one is stronger, and one is not detected.

3.3.2. B-like: Ar XIV

The conversion factor between measured signal and CHIANTI model line intensity for Ar XIV, especially the strongest line, $2s^2 2p \ ^2P_{3/2}^o-2s2p^2 \ ^2P_{3/2} \ \lambda 187.96$ is about one. A somewhat higher or moderately lower factor applies to several other lines. The higher factors suggest (unidentified) line blends, while the two cases of lower factors may suggest minor modifications to the model. The spectrometer responsivity function should not affect closely spaced line pairs, but there is no small-step proof of the smoothness of the spectrometer responsivity curve. The isoelectronic case of Ca XVI shows a similar (though weaker) enhancement of the short-wavelength lines and a weaker signal for the long-wavelength lines. Whether this gross feature results from the sensitivity function of the spectroscopic system or from the modeling, it provides an internal consistency check of the measurement.

3.3.3. C-like: Ar XIII

The conversion factor between measured signal and CHIANTI model line intensity for Ar XIII is about 0.4. Several lines in our spectra match this ratio of observation and model, which corroborates the line identifications, the model, and the assumption of a measurement only negligibly affected by line blends. When both Ar and Ca are present, two pairs of lines, in each case of Ar XIII and of Ca XIII, are partly blended with each

other at $\lambda 161.7$ and $\lambda 161.8$, and at $\lambda 162.98$, respectively. In the first case, the change of wavelength can be traced along the timeline in the discharge, but the data are not statistically reliable enough to establish individual line intensities of the components of the blend at a given time.

3.3.4. N-like: Ar XII

The conversion factor between measured signal and CHIANTI model line intensity for Ar XII is about 0.5, judging from the CHIANTI model for the strongest line, $2s^2 2p^3 \ ^2D_{5/2}^o - 2s 2p^4 \ ^2P_{3/2}$, at $\lambda 154.5$. However, just as with the isoelectronic spectrum Ca XIV, the model predicts a fair number of lines in the same ballpark of relative intensities, and our observations scatter notably for several of these lines. Others are affected by line blends, so that Ar XII does not seem to be very suitable for diagnostic studies yet. In the wavelength interval 160–170 Å there are several Ar XII lines predicted that do not exceed our detection threshold.

3.3.5. O-like: Ar XI

The conversion factor between measured signal and CHIANTI model line intensity for Ar XI is about 0.35, as indicated by the purportedly strongest Ar XI line, $2s^2 2p^4 \ ^1D_2 - 2s 2p^5 \ ^1P_1^o$ at $\lambda 151.9$, and supported by the Ar XI line $2s^2 2p^4 \ ^3P_2 - 2s 2p^5 \ ^3P_2^o$ at $\lambda 188.8$. Several lines that CHIANTI predicts at moderate intensity are not seen here, but have been corroborated in an EBIT measurement (Träbert et al. 2014b).

3.3.6. F-like: Ar X

CHIANTI predicts the $2s^2 2p^5 \ ^2P_{3/2}^o - 2s 2p^6 \ ^2S_{1/2}$ line we measure to be at $\lambda 165.5$ line as the strongest line in the Ar X EUV spectrum. If the line had the wavelength given by CHIANTI ($\lambda 166.3655$), it would be fully blended with one of the strongest Ca XIV lines (according to CHIANTI) at $\lambda 166.3455$. In our experiment, we find that the Ar X line is blended with a much weaker Ar XIII line, but the Ar X line dominates the blend. The line position of the blend is close to the literature value given by Kelly (1987), who lists a wavelength of 165.538 Å (see also Deutschman & House (1966) with wavelengths 165.53 and 170.63 Å for the line doublet). High-resolution EBIT work by Beiersdorfer & Träbert (2017) has corroborated that much earlier work. Evidently, the corresponding records in CHIANTI, for both lines of the Ar X ground-state transition multiplet, are wrong. The aforementioned line blend suggests a conversion factor between the laboratory measurement signal and the CHIANTI model prediction on the order of 0.4. The unblended second component of the same Ar X line doublet $2s^2 2p^5 \ ^2P_{3/2,1/2}^o - 2s 2p^6 \ ^2S_{1/2}$ ($\lambda 170.642$ according to Kelly (1987), Beiersdorfer & Träbert (2017), and this work; $\lambda 171.5204$ according to CHIANTI) yields a conversion factor of 0.2. Thus there is a notable mismatch of CHIANTI with observation, not only with respect to wavelengths, but also with respect to predicted intensities for this charge state.

3.3.7. Ne-like: Ar IX, Na-like: Ar VIII, Mg-like: Ar VII

We are unable to confirm any line from these charge states. CHIANTI predicts a weak Ar IX line at $\lambda 163.6355$. The line nearest to this wavelength in our spectra is at $\lambda 165.58$ and is much stronger. Judging by the observed line intensity, this line is

of unknown identity. Ar IX is Ne-like, hence the spectra with additional electrons should have a filled $n = 2$ shell and ground configurations with $3s$ electrons. CHIANTI predicts a pair of rather weak Ar VIII lines from $3p-4s$ transitions near $\lambda 230$. If our observation of a weak line at one of the two wavelengths is meaningful, the other line is missing. Thus we have no positive evidence of Ar VIII lines in our data. For Ar VII, the NIST ASD database lists a $3s-4p$ transition at $\lambda 175.5$, a position at which we see a weak line only. For the CHIANTI tables, however, this wavelength is below their range of coverage. In contrast, they list an Ar VII $3p-4s$ line at $\lambda 279.1890$, where we do not see any line.

3.4. Other Lines

In Table 3, we list lines that appear in the same plasma phase as the Ca lines discussed above, but that we cannot assign to either Ca or Ar. From the timeline of the signal we take hints whether the lines are likely unidentified leftovers of contaminants such as Mo, possibly connected to the laser injection (F, Ca), or permanently present (such as Ar). Several of the lines ($\lambda 128.45$, $\lambda 134.85$, $\lambda 166.16$, $\lambda 221.85$) have a signal that is as large as that of strong identified lines. We list these signals, because they may be helpful in a future analysis of similar Ca and Ar spectra.

4. Discussion

Tokamaks are proven light sources suitable for measuring spectra of astrophysical relevance. Injecting specific elements by laser pulse into a plasma dominated by hydrogen is a proven technique, and the combination of wavelength spectra and good time resolution permits a certain degree of discrimination of the signal against foreign contributions. The present Ca experiment focused on injection times after the initial plasma formation process with a strong contribution from Mo had passed. However, because the spectra of Mo are not sufficiently well known, it is not clear whether unidentified lines emanate from Ar or Ca or from Mo. In any case, a number of blends with unidentified lines affect the present work detrimentally.

In the present measurements, Ar was used as a tracer gas throughout the discharge. Ar demonstrated that the discharge is well suited to produce ions of similar atomic number in the right charge state range wanted for Ca, and thus the Ar EUV spectrum was available alongside that of Ca. This similarity helps to analyze the spectra and to recognize peculiarities of the spectrum model (CHIANTI) versus line blends or the appearance of foreign lines. Unfortunately, Ar with its many spectral lines (many of them useful as references) is not only rather similar to Ca, but it causes numerous line blends with Ca. Thus higher spectral resolution would be valuable for future work. We note that a very high-resolution EUV spectrometer is now available for such measurements on tokamaks (Widmann et al. 2014). Moreover, a study that attempted to clarify the spectrum of Ca near $\lambda 125$ (Träbert et al. 2014a) has produced a fair number of spectral lines and indications of the associated ionization thresholds; however, in the present study none of those lines have been confirmed as originating from Ca.

There are differing amounts of EUV spectral data in three major data repositories considered here. The data in the CHIANTI model overall prove to be the most comprehensive and up-to-date and thus are highly useful. Some mistakes in the wavelength data are noted, and we cannot corroborate any of

CHIANTI's extensive holdings of "unverified" theoretical atomic data. Of the numerous discrepancies concerning particular line intensities in the Alcator spectra most hint at line blends, whereas some others suggest shortcomings of the CHIANTI model or monotonic changes in the instrumental responsivity. We conclude that most of the seeming inconsistencies are due to the complexity of the spectra. Ca XIV, in particular, will need a closer look.

This work was performed under the auspices of the U.S. Department of Energy by Lawrence Livermore National Laboratory under Contract DE-AC52-07NA27344 and supported by the Basic Plasma Science initiative of the DOE Office of Fusion Energy Sciences.

ORCID iDs

Elmar Träbert  <https://orcid.org/0000-0002-3949-0372>

Peter Beiersdorfer  <https://orcid.org/0000-0003-0127-599X>

References

- Beiersdorfer, P. 2003, *ARA&A*, **41**, 343
- Beiersdorfer, P., Brown, G. V., Kamp, J. B., et al. 2011, *CaJPh*, **89**, 653
- Beiersdorfer, P., Lepson, J. K., Brown, G. V., et al. 1999, *ApJL*, **519**, L185
- Beiersdorfer, P., Lepson, J. K., Desai, P., et al. 2014a, *ApJS*, **210**, 16
- Beiersdorfer, P., & Träbert, E. 2017, *ApJ*, **854**, 114
- Beiersdorfer, P., Träbert, E., Lepson, J. K., Brickhouse, N. S., & Golub, L. 2014b, *ApJ*, **788**, 25
- Del Zanna, G., Dere, K. P., Young, P. R., Landi, E., & Mason, H. E. 2015, *A&A*, **582**, 56
- Dere, K. P., Landi, E., Mason, H. E., Monsignori Fossi, B. C., & Young, P. R. 1997, *ApJS*, **125**, 149
- Dere, K. P., Landi, E., Young, P. R., et al. 2009, *A&A*, **498**, 915
- Deutschman, W. A., & House, L. L. 1966, *ApJ*, **144**, 435
- Ekberg, J. O., Feldman, U., Seely, J. J., et al. 1991, *PhysS*, **43**, 19
- Feldman, U., 2016, *JPhB*, **49**, 144003
- Foster, A. R., Ji, L., Smith, R. K., & Brickhouse, N. S. 2012, *ApJ*, **756**, 128
- Graf, A. T., Brockington, S., Horton, R., et al. 2008, *CaJPh*, **86**, 307
- Hill, K. W., Bitter, M. L., Scott, S. D., et al. 2008, *RSci*, **79**, 10E320
- Howard, N. T., Greenwald, M., & Rice, J. E. 2011, *RSci*, **82**, 033512
- Jupén, C., Denne, B., & Martinson, I. 1990, *PhysS*, **41**, 669
- Kaastra, J. S., Mewe, R., & Nieuwenhuijzen, H. 1996, in 11th Coll. UV and X-ray Spectroscopy of Astrophysical and Laboratory Plasmas, ed. K. Yamashita & T. Watanabe (Tokyo: Universal Academy Press), 411
- Kelly, R. L. 1987, *JPCRD*, **16**, 1
- Kramida, A., Ralchenko, Yu., Reader, J. & NIST ASD Team 2017, NIST Atomic Spectra Database v.5.3 (Gaithersburg, MD: National Inst. Standards Tech.), <http://physics.nist.gov/asd>
- Landi, E., Del Zanna, G., Young, P. R., Dere, K. P., & Mason, H. E. 2012, *ApJS*, **744**, 99
- Landi, E., Young, P. R., Dere, K. P., Del Zanna, G., & Mason, H. E. 2013, *ApJS*, **763**, 86
- Lepson, J. K., Beiersdorfer, P., Behar, E., & Kahn, S. M. 2003, *ApJ*, **590**, 604
- Lepson, J. K., Beiersdorfer, P., Behar, E., & Kahn, S. M. 2005a, *ApJ*, **625**, 1045
- Lepson, J. K., Beiersdorfer, P., Behar, E., & Kahn, S. M. 2005b, *NIMPB*, **235**, 131
- Lepson, J. K., Beiersdorfer, P., Bitter, M., Roquemore, A. L., & Kaita, R. 2013, *PhST*, **156**, 014075
- Lepson, J. K., Beiersdorfer, P., Clementson, J., et al. 2010, *JPhB*, **43**, 144018
- Lepson, J. K., Beiersdorfer, P., Clementson, J., et al. 2012, *RSci*, **83**, 10D520
- Lepson, J. K., Beiersdorfer, P., Kaita, R., Majeski, R., & Boyle, D. 2016, *RSci*, **87**, 11D614
- Marmar, E. S. 2007, *Fus. Sci. Tech.*, **51**, 261
- Marmar, E. S., Baek, S. G., Barnard, H., et al. 2015, *NucFu*, **55**, 104020
- Raassen, A. J. J., Mewe, R., Audard, M., et al. 2002, *A&A*, **389**, 228
- Reinke, M. L., Beiersdorfer, P., Howard, N. T., et al. 2010, *RSci*, **81**, 10D736
- Rice, J. E., Terry, J. L., Fournier, K. B., et al. 1996, *JPhB*, **29**, 2191
- Rice, J. E., Terry, J. L., Marmar, E. S., et al. 2007, *Fus. Sci. Tech.*, **51**, 357
- Smith, R. K., Brickhouse, N. S., Liedahl, D. A., & Raymond, J. C. 2001, *ApJL*, **556**, L91
- Träbert, E., Beiersdorfer, P., Brickhouse, N. S., & Golub, L. 2014a, *ApJS*, **211**, 14
- Träbert, E., Beiersdorfer, P., Brickhouse, N. S., & Golub, L. 2014b, *ApJS*, **215**, 6
- Victor, B. S., Allen, S. L., Beiersdorfer, P., & Magee, E. W. 2017, *JInst*, **12**, CO6011
- Weller, M. E., Beiersdorfer, P., Soukhanovskii, V. A., Magee, E. W., & Scotti, F. 2016, *RSci*, **87**, 11E324
- White, H. E., & Eliasson, A. Y. 1933, *PhRv*, **44**, 753
- Widmann, K., Beiersdorfer, P., Magee, E. W., et al. 2014, *RSci*, **85**, 11D630